# Strain-enhanced electronic ordering in $La_3Ni_2O_7$ thin films

Arpita Mitra[1 †], David Yang[1], Claudio Mazzoli[2], Anthony T. Bollinger[1], Xi He[1], Ivan Božović[1,3] and Ian K. Robinson[1,4 †]

[1]Condensed Matter Physics and Materials Science Department, Brookhaven National Laboratory, Upton, New York 11973, USA.

[2]National Synchrotron Light Source II, Brookhaven National Laboratory, Upton, New York 11973, USA.

[3]Shanghai Advanced Research in Physical Sciences (SHARPS), Pudong, Shanghai 201203, China

[4]London Centre for Nanotechnology, University College London, WC1E 6BT, UK

The bilayer nickelate $La_3Ni_2O_7$ has recently emerged as a focal point in correlated-electron physics due to the discovery of high-temperature superconductivity under pressure and strain. At ambient pressure, this material exhibits complex density-wave instabilities governed by strong electronic correlations and orbital-selective physics. In this work, we employ coherent soft X-ray scattering (CSX) at the Ni $L_3$ edge to investigate strain-enhanced electronic ordering in $La_3Ni_2O_7$ thin films. By utilizing $SrTiO_3$ substrates to impose a large (+1.9%) tensile strain, we reveal a significantly enhanced in-plane correlation length of $\xi_{\parallel} \approx 77$ nm, more than twice that of films grown under lower-strain states. The observed superstructure peak at Q = (±0.25, ±0.25, L) shows a sharp resonance at 852 eV, confirming its origin in Ni 3d states. Analysis of the peak morphology reveals a strongly anisotropic correlation volume, where the out-of-plane correlation $\xi_{\perp} \approx 16$ nm is limited by the film thickness, indicating an ordered state that is coherent across the entire bilayer lattice. Furthermore, coherent scattering measurements reveal static speckle patterns, providing direct evidence of a nanoscale domain structure. Our findings demonstrate that epitaxial tensile strain serves as a powerful tuning parameter to stabilize long-range electronic order and to probe the interplay among charge, spin, and lattice degrees of freedom in the parent state of nickelate superconductors.

## Introduction

The Ruddlesden–Popper (RP) nickelate series $\mathrm{La_{n+1}Ni_nO_{3n+1}}$ has emerged as a new frontier in correlated-electron physics following the discovery of high-temperature superconductivity in the bilayer member $\mathrm{La_3Ni_2O_7}$ under high pressure ($T_C$ = 80 K) [1–3] and, more remarkably, at ambient pressure conditions under compressive strain ($T_C$ = 42 K) [4,5]. The phenomenon of high-$T_c$ superconductivity in layered transition-metal oxides has long motivated exploring the interplay among charge, spin, orbital, and lattice degrees of freedom. This finding situates the nickelates alongside the cuprates as systems where unconventional superconductivity may emerge from a complex landscape of intertwined orders, including charge-density waves and pair-density waves [6–9].

In both cuprates and nickelates, collective electronic correlations manifest as periodic modulations of charge and spin density, giving rise to superlattice reflections at characteristic incommensurate wave vectors. In the cuprates, these modulations appear as incommensurate satellites displaced from the antiferromagnetic wave vector $\left(\frac{1}{2},\frac{1}{2},L\right)$, corresponding to a real-space periodicity of approximately four lattice spacings, whereas in layered nickelates such as $\mathrm{La_{2-x}Sr_xNiO_4}$ the ordering wave vectors shift toward commensurate positions near $(1/3,1/3,L)$, reflecting a balancing between electronic correlations and lattice coupling [10-12]. This difference reflects the distinct balance between Coulomb and exchange interactions, as well as the orbital occupancy of the Ni 3d states, which gives rise to a qualitatively different electronic structure and ordering tendencies in nickelates.

In a recent study of ordering phenomena in metallic nickelates, Zhang *et al.* demonstrated the coexistence of spin and charge density wave correlations in $\mathrm{La_4Ni_3O_{10}}$, showing that the observed modulations are itinerant in nature and likely driven by Fermi-surface instabilities rather than by localized static stripe order [13]. More recently, density functional theory and symmetry analysis by Zhang *et al.* predicted a coupled spin–charge–orbital ordered ground state in superconducting nickelates, demonstrating that orbital polarization and bilayer coupling play a central role in stabilizing intertwined magnetic and charge orders and for generating an intrinsically entangled spin–charge–orbital ground state [13]. Together, these studies highlight that ordering phenomena in layered nickelates are inherently multicomponent, with spin, charge, and orbital degrees of freedom intertwined, and tunable by dimensionality and epitaxial strain.

Broader investigations into $La_{2-x}Sr_xNiO_4$ have highlighted the dominance of charge-driven physics, in which charge condensation and strong electron-phonon coupling (EPC) facilitate domain pinning to the lattice, driving stripe formation. Using ultrafast mid-infrared spectroscopy, Coslovich *et al.* [15] identified electronic localization as a dynamic precursor to stripe formation below $T \approx 250$ K. This state is marked by an infrared pseudogap and an enhanced Fano asymmetry in Ni-O stretch vibrations, revealing a synchronous, sub-picosecond modulation of electron-phonon coupling and charge localization. Shen *et al.* demonstrated that in $La_{2-x}Sr_xNiO_4$, charge order (CO) exhibits superior temporal stability and robust domain memory compared to spin order, with CO speckle patterns remaining even after thermal cycling to 250 K [16]. These findings identify charge condensation as the predominant driving force for stripe formation, facilitated by EPC-mediated pinning of charge domains to the lattice or structural disorder. These results provide a framework for understanding the interplay between charge, spin, and lattice degrees of freedom and the resulting density-wave instabilities in the bilayer $La_3Ni_2O_7$ system.

Optical spectroscopy [17] measurements further emphasize the role of strong electronic correlations in $La_3Ni_2O_7$, placing the material near the Mott limit, where a transition at $T \approx 115$ K opens an orbital-selective partial gap. The gap selectively suppresses the non-Fermi-liquid $3d_{z^2}$ states, while the $3d_{x^2-y^2}$ channels remain unaffected, underscoring the dominant role of $3d_{z^2}$ orbitals in the system's electronic and magnetic instabilities, consistent with recent dynamical mean-field theory calculations that predict orbital-selective correlations in bilayer nickelates [18]. Utilizing XAS and RIXS at ambient pressure, Chen *et al* [19] have established the existence of a quasi-static spin-density-wave (SDW) order in $La_3Ni_2O_7$ at the wavevector $Q = (0.25, 0.25, L)$ below 150 K. This magnetic state is governed by dispersive, optical-like magnons and reveals an inter-layer magnetic coupling an order of magnitude stronger than intra-layer interactions. This robust inter-layer exchange is driven by the strong molecular bonding of Ni $3d_{z^2}$ orbitals, a defining feature of the bilayer nickelate electronic structure. Recent RIXS investigations across the $Nd_{n+1}Ni_nO_{3n+1}$ series ($n = 1, 3, 5$) further demonstrate that structural tuning of the layer number ($n$) acts as self-doping, systematically modifying magnetic superexchange and electronic properties [20].

When stabilized as epitaxial thin films, this bilayer nickelate develops anisotropic stripe-like correlations and possible spin–charge coupling, as demonstrated by Gupta *et al.* through resonant soft x-ray scattering [21]. In that work, $La_3Ni_2O_7$ films grown under tensile strain (+0.6%) on $NdGaO_3$ (NGO) substrates have revealed modulation vectors near $(1/4, 1/4, L)$ signaling antiferromagnetic ordering accompanied by coupled charge/spin and orbital correlations. Epitaxial strain thus serves as an additional tuning parameter in thin-film nickelates, directly influencing Ni–O bond lengths and octahedral tilting, which in turn control the electronic bandwidth and correlation strength. The use of epitaxial strain to drastically modify the ground state of complex oxides is well-established, as famously demonstrated by the enhancement of ferroelectricity in strained $BaTiO_3$ [22]. Following this paradigm, we explore higher tensile strain levels in bilayer nickelates to stabilize long-range order. In this work, we examined films grown on $SrTiO_3$ (STO) substrates, which subject the bilayer lattice to a significantly higher tensile strain of +1.9 %, providing a contrast to the lower strain state imposed by NGO. This investigation could answer a key question whether the epitaxial strain alters the coupling between magnetic and structural correlations or can these degrees of freedom evolve independently. The degree of spin and charge ordering can both be quantified by their robustness against thermal excitation, typically through the phase transition temperature. They can also be documented by the correlation lengths of antiferromagnetism and charge ordering.

Here we employed Coherent X-ray Scattering (CXS) at the National Synchrotron Light Source II (NSLS-II) at the Ni $L_3$ edge to directly probe nanoscale correlations in epitaxial $La_3Ni_2O_7$ films. CXS preserves the X-ray beam coherence, hence the phase interference of the scattered field, allowing the analysis of speckle patterns [23]. The coherence makes the scattering uniquely sensitive to the sample's local disorder, domain morphology, and temporal dynamics, as revealed by these speckle patterns [24, 25]. This capability allows us to directly quantify the spatial correlation length and precisely measure characteristic lineshapes (commensurate vs. incommensurate) with high resolution [26, 27]. We present our experiments on $La_3Ni_2O_7$ films grown on an $SrTiO_3$ (STO) substrate to determine whether the increased epitaxial tensile strain, compared to NGO, modifies the magnetic and structural correlation, thereby measuring the degree of coupling between lattice and spin order in this layered nickelate system. Our results show enhanced structural coherence as evidenced by speckle features and larger correlation lengths. This demonstrates that epitaxial tensile strain promotes improved ordering and more coherent domains of coupled electronic and lattice correlations in this layered nickelate, providing a new route to manipulate intertwined orders in correlated-electron systems through substrate boundary conditions.

## Experimental Method

Epitaxial thin films of the Ruddlesden–Popper (RP) phase $La_3Ni_2O_7$ were synthesized using atomic layer-by-layer Molecular beam epitaxy (ALL MBE) technique. The growth of epitaxial RP phase nickelate films using MBE and pulsed laser deposition (PLD) has been previously established [4, 28-31]. The target thickness for our films is 20 monolayers (ML), corresponding to $h \approx 20$ nm. Epitaxy depends on the choice of substrates. Here we employed single-terminated crystal $SrTiO_3$ (STO) substrates, which are cubic perovskites with lattice constant $a = 3.905$ Å. All were commercially sourced and polished perpendicular to the crystallographic [001] direction. The as-received substrates were insulating. The film was deposited at a substrate temperature of 800 C in an ozone atmosphere with a pressure maintained at $3 \times 10^{-5}$ mbar. Following the completion of 20 cycles, the films were cooled down to 250 C at a rate of 20 C/min. During this cooling stage, we increased the ozone partial pressure to $1 \times 10^{-4}$ mbar to ensure proper oxygen stoichiometry in the Ni-O bilayers. Due to lattice mismatch, $La_3Ni_2O_7$ films grown on STO exhibit a tensile strain of +1.9 % [32] and remain coherently strained and epitaxially anchored to the substrate (pseudomorphic growth). During the growth, reflection high-energy electron diffraction (RHEED) was used for *in situ* monitoring of the surface structure and layer-by-layer growth, ensuring stoichiometric and epitaxial control at the monolayer level. The crystalline structure of the films was characterized by x-ray diffraction (XRD) using a Bruker D8 diffractometer, while the surface morphology and roughness were probed by atomic force microscopy (AFM), shown in Supplementary Fig. S1.

Coherent and incoherent resonant soft X-ray scattering experiments were conducted at the Coherent Soft X-ray (CSX) beamline of the National Synchrotron Light Source II (NSLS-II) at Brookhaven National Laboratory. The measurements were performed at the Ni $L_3$ absorption edge (~852 eV). The spatial coherence and instrumental resolution were controlled by the monochromator's 50 μm "exit" pinhole aperture positioned upstream of the sample. For incoherent measurements, the 50 μm pinhole was placed in front of the sample, while the coherent scattering measurement was achieved by utilizing an 8 μm pinhole, 6 mm in front of the sample, to define a coherent illumination area on the sample. The diffracted x-ray intensity was recorded using the newly implemented AXIS detector mounted on the γ/δ arm of the CSX end station in-vacuum diffractometer, enabling high dynamic range and angular resolution, given by its 9 μm pixel size. The exit slit of the monochromator determined the energy resolution, while the pinhole size set the beam footprint and transverse coherence length at the sample. The detector was placed in the specular configuration to calibrate the zero angle of the sample and set the "half-height" position at the 100 K measurement temperature before locating the off-specular diffraction peaks.

## Results

Resonant soft x-ray scattering measurements were carried out at a fixed photon energy corresponding to the Ni $L_3$ absorption edge (≈ 852 eV), where the incident and scattered wave vectors define the momentum transfer vector **Q** in reciprocal space. Fig. 1 illustrates the scattering geometry in reciprocal-space coordinates. The in-plane and out-of-plane components of the momentum transfer are denoted as $Q_{\parallel}$ and $Q_{\perp}$, respectively.

Two distinct scattering geometries were employed to access the positive and negative peak positions (±0.25, ±0.25, L) along the in-plane direction. For each setting, the $\mathbf{Q} = \mathbf{k_f} - \mathbf{k_i}$ diffraction triangles lie close to the plane shown. The area-detector plane, tangent to the Ewald sphere, is shown as a line perpendicular to the $\mathbf{k_f}$ vector direction in each case, Setting I corresponds to a near-grazing-incidence configuration (θ = 13°), in which the detector cut emphasizes the in-plane component $Q_{\parallel}$, whereas Setting II corresponds to near-normal incidence (θ = 110°), probing the same modulation from the opposite side of reciprocal space. The fixed photon energy determines the radius of the Ewald sphere, shown schematically by the intersection of the incident and scattered wave vectors with the reciprocal lattice. The measurements were performed under identical energy and detector angle settings for both Setting I and II geometries.

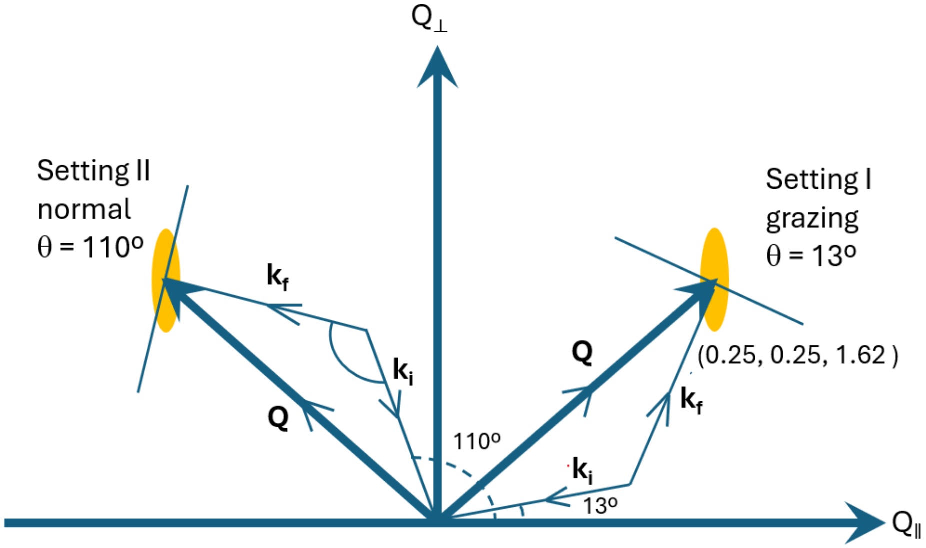

FIG. 1. Schematic scale reciprocal space drawing of the scattering geometry illustrating the relationship between the incident and scattered wave vectors and the resulting momentum transfer **Q**. The in-plane and out-of-plane components, $Q_\parallel$ and $Q_\perp$, define the measurement coordinate system. Two settings were used: Setting I (near-grazing incidence, θ = 13°) and Setting II (near-normal incidence, θ = 110°). Yellow ellipses indicate the position and shape of the Bragg peak.

Following this geometric configuration, reciprocal-space maps were collected in both scattering settings to probe the charge ordering. The scattered intensity exhibits a well-defined peak centered at the expected in-plane momentum transfer, (±0.25, ±0.25, *L*) at *L*=1.62. Probing the correlation along the out-of-plane direction, $Q_\perp$, was limited by the geometry of the Ewald sphere at fixed photon energy. The intersection of the Ewald sphere with reciprocal space is too steep to allow meaningful *L*-scans at the Ni $L_3$ edge. As a result, the measurement primarily integrates over a narrow range in $Q_\perp$ and no measurable variation in intensity along *L* was observed over the limited accessible scan range. To verify the resonant behavior of the peak, we performed an energy scan while adjusting the diffraction angles to keep a fixed scattering vector **Q**. The scattered intensity as a function of photon energy, shown in Fig. 2, exhibits a distinct resonance feature centered near the Ni $L_3$ absorption edge, confirming that the scattering originates from electronic ordering associated with Ni 3d states in the film.

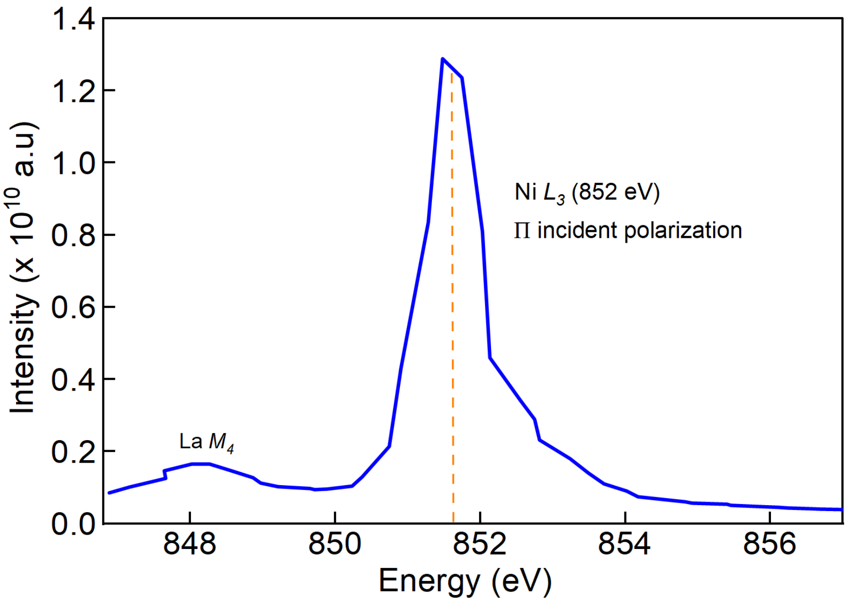

FIG. 2. Energy-dependent resonant soft x-ray scattering intensity measured at fixed momentum transfer **Q**. The scattered intensity shows a sharp resonance centered near 852 eV, coinciding with the Ni $L_3$ ($2p_{3/2} \rightarrow 3d$) absorption edge, confirming that the scattering arises from Ni 3d electronic states associated with the ordered phase in $La_3Ni_2O_7$.

The scattering intensity profile was analyzed to determine the structural characteristics and correlation lengths of the observed superstructure Bragg peak. A representative 2D intensity map of the peak in setting II (Fig. 1) is shown in Fig. 3a. The peak shape is elliptical, consistent with scattering from a thin-film structure where the in-plane and out-of-plane correlation lengths are different [33]. To quantify the peak dimensions, we extracted the horizontal and vertical line profiles along the directions of the $Q_{\parallel}$ and $Q_{\perp}$ components, respectively as shown in Fig. 3b and 3c.

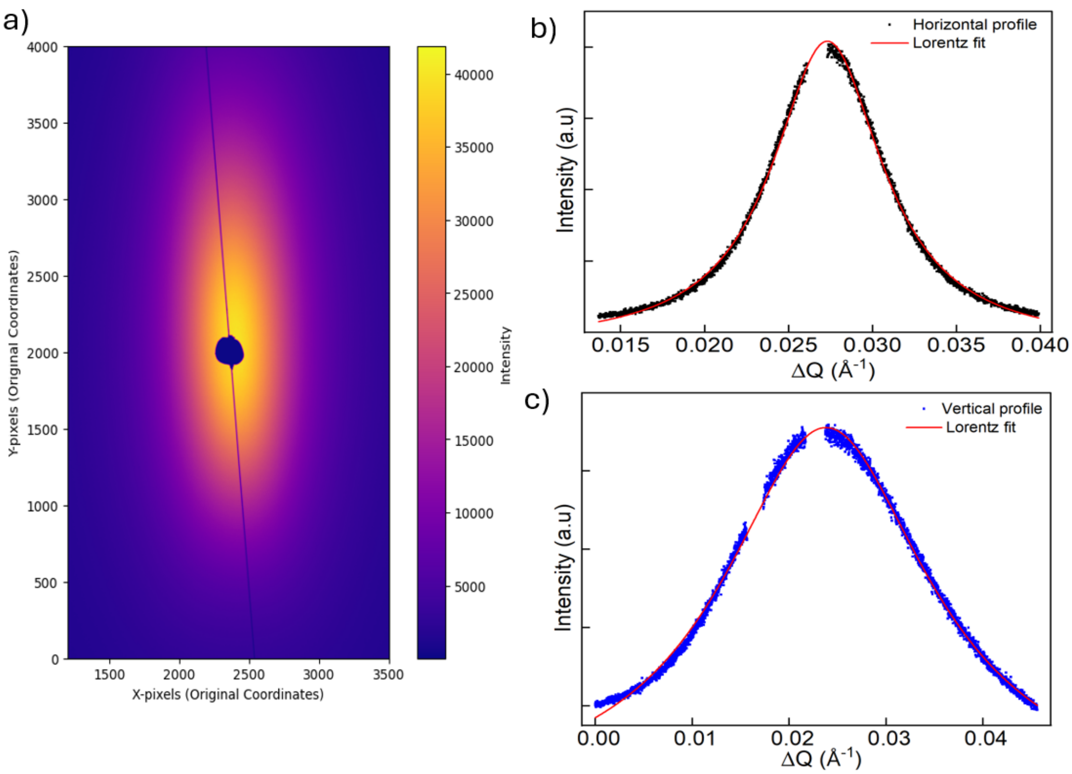

FIG. 3. (a) The left panel shows the 2D intensity map of the observed Bragg peak in detector coordinates (pixels). The peak is elliptical shaped along the vertical direction, indicating a strong anisotropy between the in-plane and out-of-plane structural correlation lengths. (b) and (c) The right panels display the line profiles extracted along the horizontal and vertical directions.

Both the profiles are fitted with a Lorentzian function (red line) to determine the Full Width at Half Maximum (FWHM). The measured FWHM values obtained from the line profiles were converted into reciprocal space units ($\Delta Q_{\mathrm{FWHM}}$) and then into real-space correlation lengths ($\xi$). The calculation uses the relationship for small angles in reciprocal space:

$$\Delta Q_{FWHM} \approx \frac{2\pi}{\lambda} . \frac{p.s}{d} \tag{1}$$

where $p$ is FWHM in pixels, $s$ is the pixel size (9 µm), $d$ is the sample-detector distance (0.3 m) and $\lambda$ is the wavelength (1.65 nm).

The correlation length ($\xi$) for a Lorentzian lineshape is calculated using the Scherrer-like relationship:

$$\xi = \frac{2\pi}{\Delta Q_{\mathrm{FWHM}}} \tag{2}$$

The line profiles extracted along the horizontal and vertical directions for setting II, when fitted with a Lorentzian function (red line), yield FWHM of 717 pixels for the horizontal profile and 2285 pixels for the vertical profile. The horizontal profile, representing the in-plane order, yielded a long in-plane correlation length of about 77 nm, substantially larger than previously reported values [19, 21]. This value confirms a high degree of crystalline order and large domain size within the scattering plane.

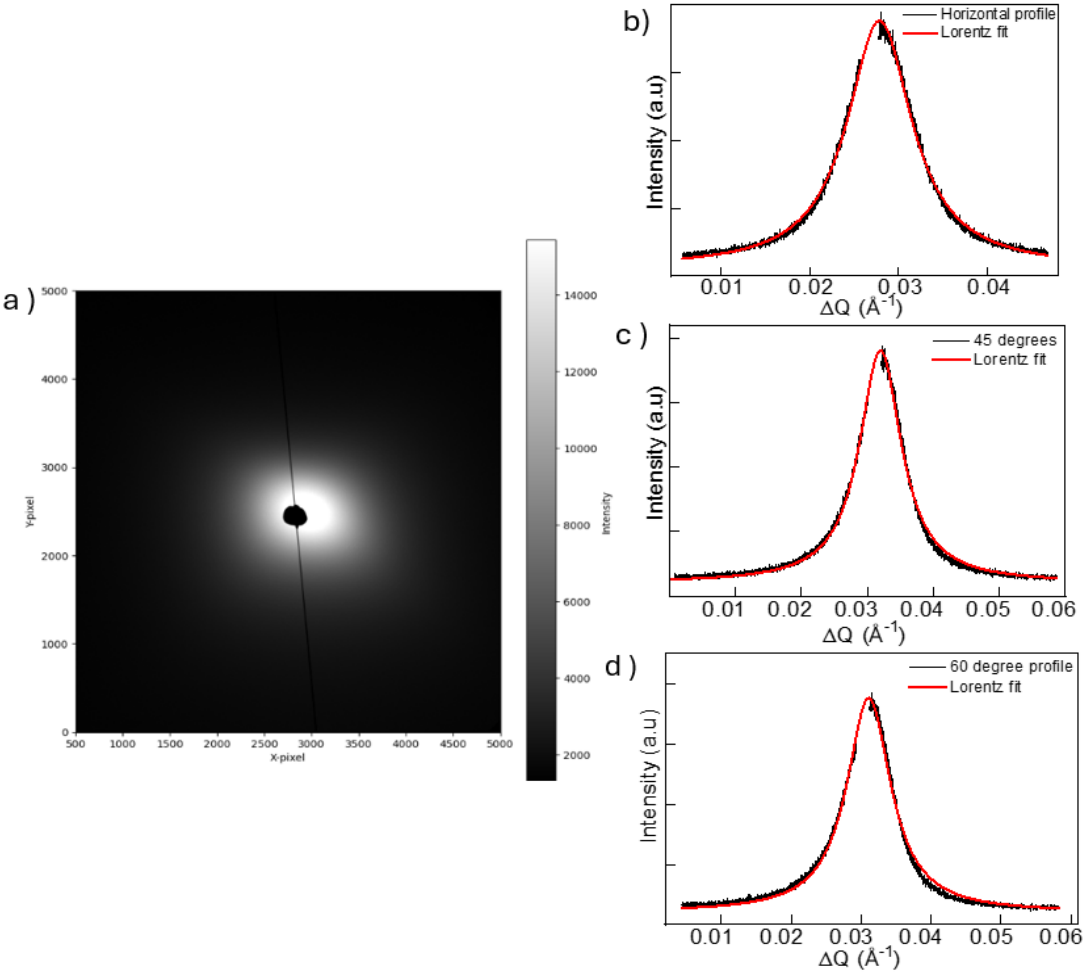

FIG. 4. (a) 2D intensity map of the (0.25, 0.25, L) Bragg peak for the setting I. (b–e) Line profiles of the Bragg peak intensity extracted along three directions: (b) horizontal, (c) 45°, and (d) 60°. Experimental data are shown as black dots, and Lorentzian fits are overlaid in red.

For Setting I, Fig. 4a displays the two-dimensional intensity map with the near-grazing-incidence geometry (θ = 13°) to probe the in-plane modulation. To quantify the peak shapes and extract spatial correlation information, line profiles were extracted along the horizontal, vertical, 45°, and 60° directions. As shown in Fig. 4b - d, these profiles are also well-described by Lorentzian fits, allowing for the precise determination of FWHM in both pixel and reciprocal space units ($\Delta Q_{FWHM}$). The extracted parameters for Setting I reveal a directional dependence in the spatial correlations. Specifically, the horizontal profile yielded a correlation length of 71 nm whereas the vertical, 45°, and 60° profiles exhibited a larger correlation length of about 80 nm. This subtle anisotropy in Setting I is inherently linked to an approximately square shape of the ordered domains, rather than round. These findings at +**Q** provide a quantitative baseline for comparison with Setting II (θ = 110°), which accesses the conjugate **-Q** peak position at near-normal incidence to ensure a complete characterization of the reciprocal space modulation. Importantly, the close agreement between $\xi_{\parallel}$ obtained in Settings I and II demonstrates that the lateral correlation length is an intrinsic property of the film. Table 1 presents the summary of the fitted values obtained from the line profiles for setting I and setting II scattering geometries.

Table 1: Summary of fitted FWHM values, reciprocal-space widths ($\Delta Q_{\mathrm{FWHM}}$), and extracted correlation lengths ($\xi$) for different measurement directions and geometries.

| Setting II | | | |
|---|---|---|---|
| Profile Direction | FWHM (pixels) | $\Delta Q_{\mathrm{FWHM}}$ (A˚−1) | Correlation Length ($\xi$) (nm) |
| Horizontal Profile | 717 | 0.00819 | 76.7 |
| Vertical Profile | 2285 | 0.02597 | 24.2 |
| Setting I | | | |
| Horizontal Profile | 778 | 0.00887 | 70.9 |
| Vertical Profile | 690 | 0.00786 | 80.0 |
| 45 degrees | 684 | 0.00781 | 80.5 |
| 60 degrees | 676 | 0.00772 | 81.4 |

The vertical profile in setting II is measured along the Ewald sphere tilted by the specific $\mathbf{k}_f$ exit angle (14°) to the true perpendicular direction of the film. To determine the true perpendicular (out-of-plane) correlation length, $\xi_\perp$ we need to deconvolute the 14° cutting of the assumed elliptical shape of the diffraction peak in reciprocal space. This slice, shown in Fig. 5, accounts for the contributions of the in-plane (parallel) $\xi_\parallel$ and out-of-plane (perpendicular) $\xi_\perp$ to the experimentally measured correlation length $\xi_{\mathrm{measured}}$ in the detector plane.

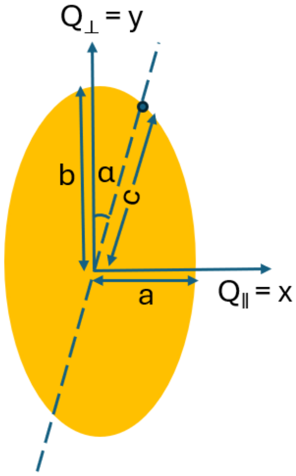

FIG. 5. Schematic illustration of the measurement directions overlaid on the elliptical shape of the (0.25, 0.25, L) diffraction peak in reciprocal space. The semi-axes $a$ and $b$ of the ellipse (half-widths) correspond to the half-width of the in-plane and out-of-plane peaks, respectively. The dashed line indicates a detector-plane line cut taken at the fixed exit angle $\alpha = 14°$, along which the experimentally measured width $c = \Delta Q_{meas}/2$ was obtained. The measured width represents a geometric cutting of the intrinsic anisotropic correlation ellipse determined by the scattering geometry.

Fig. 5 schematically illustrates the diffraction ellipse in reciprocal space where the semi-axes $a = \frac{\Delta Q_{\parallel}}{2}$ and $b = \frac{\Delta Q_{\perp}}{2}$. The ellipse is described by the equation

$$\left(\frac{x}{a}\right)^2 + \left(\frac{y}{b}\right)^2 = 1 \tag{3}$$

where x-axis and y-axis are defined along the $Q_{\parallel}$ (in-plane) and $Q_{\perp}$ (out-of-plane) directions, respectively. For a detector slice taken at an exit angle $\alpha$, the coordinates along the slice satisfy $x = c \sin\alpha\, , y = c\cos\,\alpha$, $\tan \alpha = x/y$ and $x^2 + y^2 = c^2$ where $c = \frac{\Delta Q_{meas}}{2}$ is the measured peak width. Substituting these relations into the ellipse equation:

$$b = \frac{c\cos\alpha}{\sqrt{1 - \left(\frac{c\sin\alpha}{a}\right)^2}}$$

$$\Delta Q_{\perp} = \frac{\Delta Q_{meas} \cos\alpha}{\sqrt{1 - \left(\frac{\Delta Q_{meas} \sin\alpha}{\Delta Q_{\parallel}}\right)^2}}$$

Using the independently determined in-plane $\Delta Q_{\parallel}$ = 0.00819 Å$^{-1}$ the measured value $\Delta Q_{meas}$ = 0.02597 Å$^{-1}$ along the $\alpha = 14°$ slice, we extract $\Delta Q_{\perp}$= 2b = 0.03926 Å$^{-1}$ and hence the perpendicular correlation length $\xi_{\perp} = 2\pi/\Delta Q_{\perp}$ = 16 nm.

The extracted values $\xi_{\parallel} \approx 77$ nm and $\xi_{\perp} \approx 16$ nm demonstrate a strongly anisotropic correlation volume elongated within the film plane. The out-of-plane correlation length $\xi_{\perp}$ is notably shorter and is comparable to the total film thickness (~20 nm). This constraint is a characteristic signature of thin-film scattering, where the thickness of the film imposes a finite size effect that limits the out-of-plane correlation length. [26, 33]

Coherent scattering measurements were then performed by inserting an 8 μm exit pinhole into the beam 6 mm before the sample. These reveal speckle modulations superimposed on the resonant scattering peak as shown in Fig. 6a, consistent with a nanoscale domain structure within the illuminated volume and confirm that the experiment probes the sample in the coherent scattering regime. The speckle dimensions should correspond to the illuminated footprint of the beam on the sample surface. The dynamic behavior of the domains is investigated using time-dependent measurements shown in Fig. 6b. The correlation functions from these data showed no detectable fluctuations in domain positions or sizes. Instead, they showed an exponential intensity decay under continuous illumination, with an average lifetime of about 15 seconds, as indicated by the fit shown in Fig. 6. To better visualize the intrinsic speckle morphology, Fig. 6c shows the same speckle pattern compressed along the vertical detector direction by a factor of 12. After this rescaling, the speckles appear approximately circular or spherical in shape. These observations underscore the importance of disentangling geometric and coherence effects from intrinsic sample properties when interpreting speckle patterns in grazing-incidence coherent scattering experiments.

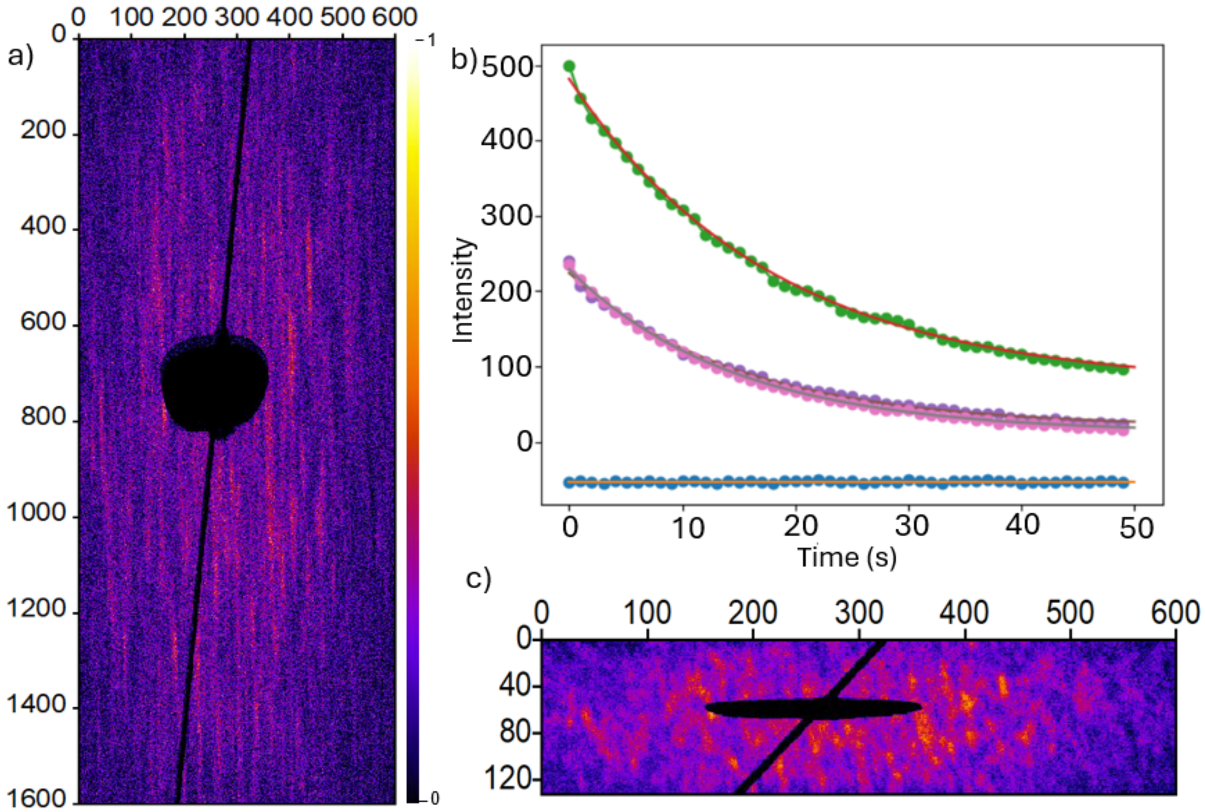

FIG. 6. (a) Coherent scattering measurements reveal speckle patterns superimposed on the Bragg peak, indicating the presence of static nanoscale domains. The axes are labeled in units of pixels, which are 9 μm wide. (b) Time-dependent scans show intensity decay attributed to beam-induced damage. (c) Speckle pattern from (a) compressed by a factor of 12 along the vertical direction, revealing the approximately spherical shapes as a way to estimate the apparent elongation in the raw data.

The expected speckle size, $\Delta x$, can be estimated from the illuminated beam footprint (diameter) on the scattering surface, D, using the optical diffraction relation:

$$\Delta x \approx \frac{\lambda d}{D} \tag{4}$$

Where $\lambda$ *is* the wavelength and $d$ is the sample-to-detector distance. Thus, speckle size is inversely proportional to the beam footprint. From the setting II scattering geometry, with $\lambda = 1.45$ nm, $d = 0.3$ m and beam Size, $D_y = 8$ μm, we expect an in-plane speckle size of $\Delta y \approx 54$ μm or 6 pixels, in good agreement with the horizontal speckle size seen in Fig. 6. The speckles should be elongated in the out-of-plane detector direction to $\Delta x \sim 224.2\,\mu$m (~ 25 pixels), due to the nearly grazing exit angle of the scattering geometry ($\alpha = 14^{\circ}$) which shortens the footprint to $D_x = 1.94$ µm. The resulting elliptical aspect ratio of the speckles is expected to be roughly 4:1 from this geometric projection.

## Discussion

The resonant soft X-ray scattering measurements reveal that the in-plane correlation lengths in the $La_3Ni_2O_7$/STO films are significantly larger than those previously reported for $La_3Ni_2O_7$ films grown on $NdGaO_3$ (NGO) substrates [21]. NGO-grown films, stabilized under lower tensile strain, show relatively short-range correlations of the order of $\xi_{\parallel} = 29$ nm and $\xi_{\perp} = 13$ nm. In contrast, our results on STO-grown films under tensile strain exhibit parallel correlation lengths exceeding 77 nm, demonstrating markedly improved lateral coherence. This enhancement indicates that tensile strain from STO promotes larger structural or magnetic domains, likely by modifying the Ni–O–Ni bond geometry, reducing octahedral rotations, and enhancing the stiffness of the ordering order parameter, in agreement with theoretical predictions on strain-tuned nickelates [16, 21]. At the same time, the crystalline quality of complex-oxide thin films is known to depend sensitively on extrinsic growth factors, including substrate surface preparation and termination, as well as the unavoidable substrate miscut, which determines step orientation, terrace width, and step density. Variations in these parameters can influence defect densities and domain nucleation and may therefore contribute to the observed enhancement of correlation length in STO-grown films in addition to the intrinsic effects of epitaxial strain. However, the out-of-plane correlation length, $\xi_{\perp} = 16$ nm for STO and 13 nm for NGO, are both comparable to the total film thickness (~20 nm). This indicates that the ordering is at least correlated across the full film thickness, with no evidence of vertical modulation decay. The energy-dependent line shape and the presence of a clear resonant peak at the Ni $L_3$ edge at fixed **Q** provides direct evidence for a well-defined electronic modulation involving Ni 3d electronic states in the film.

The extracted in-plane correlation lengths $\xi_{\parallel}$ are consistent across both measurement geometries: approximately 71 nm in the near-grazing-incidence configuration (Setting I) and 77 nm in the near-normal configuration (Setting II). Because these configurations illuminate different regions of the film and probe slightly different in-plane momentum trajectories, the small variation in correlation length likely reflects local inhomogeneity rather than a change in the intrinsic ordering mechanism.

In Setting I, the difference between $\xi_{\parallel}$ and $\xi_{\perp}$ is about 10 % which may indicate to some in-plane anisotropy of domain morphology or a variation in defect density, both of which can subtly alter the apparent correlation length, especially in a thin film where substrate miscut can be present. However, the overall correlation lengths remain large and relatively uniform, demonstrating the intrinsic robustness of the in-plane ordering stabilized by tensile strain in the STO-grown films.

Coherent scattering measurements further reveal dynamic speckle modulations superimposed on the Bragg peak, indicative of nanoscale domain structure within the illuminated volume. The speckle size, however, is determined primarily by the X-ray footprint and sample-to-detector distance, while the intrinsic domain size of the film corresponds to the envelope of the speckles, as captured by the correlation length measurements discussed above. This suggests that the domains are close packed to generate the interference seen in the formation of speckles within the envelope of the (0.25, 0.25, L) Bragg peak. Assuming the beam size on the sample is given by the 8 μm pinhole, the speckle size on the detector would be 54 μm, as observed. The speckles are dynamic only in the sense that they decay, without changing their distribution, with a lifetime of 15 sec. We observe a 12x elongation of the speckles in the perpendicular direction, of which 4x is expected from the beam footprint geometry. We consider that the additional elongation comes from the wavelength spread of the CSX monochromator ($5 \times 10^{-4}$). This demonstrates that the radial elongation of the speckles is an instrumental consequence of the finite longitudinal coherence, due to the gratings of the monochromator.

We observed irreversible decay in speckle intensity under continuous illumination, accompanied by the formation of localized burn patches, when the sample was scanned afterwards. Such beam-induced damage is plausibly attributed to oxygen loss or redistribution, which destabilizes the electronic configuration of $La_3Ni_2O_7$, a phenomenon observed in transition metal oxides where high-flux soft x-rays facilitate the reduction of high-valence metal centers [34]. RP nickelates are known to support multiple oxygen coordination environments and are more open to oxygen inter- or out-diffusion than layered cuprates, which possess more rigid, well-defined oxygen sublattices. The sensitivity of $La_3Ni_2O_7$ to X-ray damage thus reflects its metastable stoichiometry and reinforces the need for low-dose or protected-surface strategies when probing correlated ordering at soft X-ray energies.

## Conclusion:

In summary, resonant and coherent soft X-ray scattering measurements demonstrate that $La_3Ni_2O_7$ thin films grown on $SrTiO_3$ substrates exhibit substantially enhanced in-plane correlation lengths (77 nm) compared with films grown on $NdGaO_3$ under lower tensile strain. This establishes epitaxial tensile strain as a decisive control parameter for stabilizing larger and coherent ordered domains in bilayer nickelates, possibly by modifying the Ni-O-Ni bond angles and quenching octahedral rotations. The absence of measurable dispersion along the $L$ direction indicates an ordered state extending coherently across the full film thickness, with no detectable out-of-plane modulation. Because resonant scattering at the Ni $L_3$ edge is sensitive to Ni 3d valence states, the observed signal likely reflects an intertwined electronic order involving spin, charge, and orbital degrees of freedom. The observation of a single, well-defined Lorentzian lineshape suggests that the ordered state is governed by a dominant, unified ordering mechanism rather than multiple competing phases. Coherent scattering reveals a static nanoscale domain structure via well-defined speckle patterns. However, beam-induced degradation in $La_3Ni_2O_7$, possibly due to oxygen loss or surface modification, imposes practical limits on total exposure time. The observed anisotropy between the in-plane and out-of-plane speckle dimensions is primarily governed by the asymmetric scattering geometry and the instrumental coherence limits. Our analysis confirms that the speckle morphology is modified by the finite longitudinal coherence of the CSX beamline. The observed 12 times radial elongation of the speckles corresponds to the wavelength spread, $d\lambda/\lambda = 5 \times 10^{-4}$ of the CSX monochromator's energy resolution. Our results establish epitaxial strain as a powerful tuning parameter for controlling electronic ordering in bilayer nickelates and demonstrate the capability of coherent scattering to probe nanoscale ordering, while emphasizing the need for careful management of beam-induced damage in oxygen-sensitive correlated oxides. With further optimization of this experiment in the future, we should be able to achieve ptychographic imaging of the domain structure, as previously achieved in LSNO [25], noting that multiple exposures of the same sample location would be required.

## Future direction

Moving forward, we aim to explore several paths to investigate ordering in RP phase nickelates. First, *in situ* Au capping layers may mitigate surface oxygen loss and enhance sample stability under coherent x-ray illumination, allowing significantly longer exposure times. Our second goal is to perform Bragg ptychography to extract real-space maps of domain structure, utilizing advanced iterative algorithms to resolve the complex domain morphology at the nanoscale [35]. Third, exploring the growth process on additional substrates will enable a systematic exploration of the strain-correlation length landscape, enabling the role of epitaxial boundary conditions to be mapped more completely. Finally, employing asymmetric pinholes, for example, triangular ones, offer a means to break the symmetry of the probing beam and improve the diversity of spatial Fourier components in the diffraction patterns, thereby enhancing the robustness and convergence of iterative phase retrieval [24]. This previous work demonstrated single-frame coherent diffractive imaging as a practical method for mitigating the "twin-image" problem. A triangular aperture was used as a key element for the optical system. The image of a selected field of view of an extended object was obtained by phase retrieval calculation, whose spatial resolution turned was limited by both the sharpness of triangular aperture edges and the quality of the diffracted intensity pattern in the high-Q-region [36]. Together, these future directions are expected to extend the capabilities demonstrated here and open the door to high-resolution, real-space imaging of nanoscale ordering in correlated nickelates.

## Acknowledgement

The work at Brookhaven National Laboratory (BNL) was supported by the U.S. Department of Energy (DOE), Office of Basic Energy Sciences, under Contract No. DE-SC0012704. The work at UCL was supported by EPSRC and ERC. This research used the 23-ID-1 beamline of the National Synchrotron Light Source II; a U.S. DOE Office of Science User Facility operated for the DOE Office of Science by BNL under Contract No. DE-SC0012704.

## References

1. G. Wang, N. N. Wang, X. L. Shen, J. Hou, L. Ma, L. F. Shi, Z. A. Ren, Y. D. Gu, and H. M. Ma, P. T. Yang, Z. Y. Liu, H. Z. Guo, J. P. Sun, G. M. Zhang, S. Calder, J.-Q. Yan, B. S. Wang, Y. Uwatoko, and J.-G. Cheng. Pressure-Induced Superconductivity in Polycrystalline $La_3Ni_2O_7$. Phys. Rev. X 14, 011040 (2024).

2. H. Sun, M. Huo, X. Hu, J. Li, Z. Liu, Y. Han, L. Tang, Z. Mao, P. Yang, B. Wang, J. Cheng, DX. Yao, GM. Zhang, and M. Wang. Signatures of superconductivity near 80 K in a nickelate under high pressure. Nature (London) 621, 493 (2023).

3. L. Wang, Y. Li, S-Y. Xie, F. Liu, H. Sun, C. Huang, Y. Gao, T. Nakagawa, B. Fu, B. Dong, Z. Cao, R. Yu, S. I. Kawaguchi, H. Kadobayashi, M. Wang, C. Jin, H-k. Mao, and H. Liu. Structure Responsible for the Superconducting State in $La_3Ni_2O_7$ at High-Pressure and Low-Temperature Conditions. J Am Chem Soc. 146 7506-7514 (2024)

4. E. K. Ko, Y. Y, Y. Liu, L. Bhatt, J. Li, V. Thampy, C.-T. Kuo, B.-Y Wang, Y. Lee, K. Lee, J.S Lee, B.H. Goodge, D. A. Muller, and H. Y. Hwang. Signatures of ambient pressure superconductivity in thin film $La_3Ni_2O_7$. Nature 638, 935–940 (2025).

5. B. Hao, M. Wang, W. Sun, Y. Yang, Z. Mao, S. Yan, H. Sun, H. Zhang, L. Han, Z. Gu, J. Zhou, D. Ji, and Y. Nie. Superconductivity in Sr-doped $La_3Ni_2O_7$ thin films. Nat. Mater. (2025).

6. M. Vojta. Lattice symmetry breaking in cuprate superconductors: stripes, nematics, and superconductivity. Advances in Physics, 58(6), 699–820 (2009).

7. S. Anissimova, D. Parshall, G. D. Gu, K. Marty, M. D. Lumsden, S. Chi, J. A. Fernandez-Baca, D. L. Abernathy, D. Lamago, and J. M. Tranquada. Direct observation of dynamic charge stripes in $La_{2-x}Sr_xNiO_4$. Nat. Commun. 5, 3467 (2014).

8. B. Keimer, S. A. Kivelson, M. R. Norman, S. Uchida, and J. Zaanen. From quantum matter to high-temperature superconductivity in copper oxides. Nature 518, 179–186 (2015).

9. F. Eduardo, S. A. Kivelson, and J. M. Tranquada. Theory of intertwined orders in high temperature superconductors. Rev. Mod. Phys. 87, 457 (2015).

10. M. E. Ghazi, P. D. Spencer, S. B. Wilkins, P. D. Hatton, D. Mannix, D. Prabhakaran, A. T. Boothroyd, and S.-W. Cheong. Incommensurate charge stripe ordering in $La_{2-x}Sr_xNiO_4$. Phys. Rev. B 70, 144507 (2004).

11. H. Yoshizawa, T. Kakeshita, R. Kajimoto, T. Tanabe, T. Katsufuji, and Y. Tokura, Spin and charge ordering in $La_{2-x}Sr_xNiO_4$ with $0.27\leqslant x\leqslant 0.5$. Physica B 241, 880 (1997).

12. J. M. Tranquada, B. Sternlieb, J. D. Axe, Y. Nakamura, and S. Uchida. Evidence for stripe correlations of spins and holes in copper oxide superconductors. Nature 375, 561–563 (1995).

13. J. Zhang, D. Phelan, A. S. Botana, Y.-S. Chen, H. Zheng, M. Krogstad, S. G. Wang, Y. Qiu, J. A. Rodriguez-Rivera, R. Osborn, S. Rosenkranz, M. R. Norman, and J. F. Mitchell. Intertwined density waves in a metallic nickelate. Nat. Commun. 11, 6003 (2020).

14. B. Zhang, C. Xu, and H. Xiang. Spin-charge-orbital order in nickelate superconductors. Phys. Rev. B 111, 184401 (2025).

15. G. Coslovich, B. Huber, W. -S. Lee, Y. -D. Chuang, Y. Zhu, T. Sasagawa, Z. Hussain, H. A. Bechtel, M. C. Martin, Z. -X. Shen, R. W. Schoenlein, and R. A. Kaindl. Ultrafast charge localization in a stripe - phase nickelate. Nat Commun 4, 2643 (2013).

16. Y. Shen, G. Fabbris, H. Miao, Y. Cao, D. Meyers, D. G. Mazzone, T. A. Assefa, X. M. Chen, K. Kisslinger, D. Prabhakaran, A. T. Boothroyd, J. M. Tranquada, W. Hu, A. M. Barbour, S. B. Wilkins, C. Mazzoli, I. K. Robinson, and M. P. M. Dean. Charge Condensation and Lattice Coupling Drives Stripe Formation in Nickelates. Phys. Rev. Lett. 126, 177601 (2021).

17. Z. Liu, M. Huo, J. Li, Q. Li, Y. Liu, Y. Dai, X. Zhou, J. Hao, Y. Lu, M. Wang, and H. -H. Wen. Electronic correlations and partial gap in the bilayer nickelate $La_3Ni_2O_7$. Nat Commun. 15 7570 (2024)

18. V. Christiansson, F. Petocchi, and P. Werner. Correlated Electronic Structure of $La_3Ni_2O_7$ under Pressure. Phys. Rev. Lett. 131, 206501(2023).

19. X. Chen, J. Choi, Z. Jiang, J. Mei, K. Jiang, J. Li, S. Agrestini, M. Garcia-Fernandez, H. Sun, X. Huang, D. Shen, M. Wang, J. Hu, Y. Lu, J. Zhou, and Feng, D. Electronic and magnetic excitations in $La_3Ni_2O_7$. Nat Commun 15, 9597 (2024).

20. S. F. R TenHuisen, G. A. Pan, Q. Song, D. R. Baykusheva, D. F. Segedin, B. H. Goodge, H. Paik, J. Pelliciari, V. Bisogni, Y. Gu, S. Agrestini, A. Nag, M. García-Fernández, K.-J. Zhou, L. F. Kourkoutis, C. M. Brooks, J. A. Mundy, M. P. M. Dean, and M. Mitrano. Magnetic excitations in $Nd_{n+1}Ni_nO_{3n+1}$ Ruddlesden-Popper nickelates observed via resonant inelastic x-ray scattering. Phys. Rev. B 111, 165145 (2025).

21. N. K. Gupta, R. Gong, Y. Wu, M. Kang, C. T. Parzyck, B. Z. Gregory, N. Costa, R. Sutarto, S. Sarker, A. Singer, D. G. Schlom, K. M. Shen, and D. G. Hawthorn. Anisotropic spin stripe domains in bilayer $La_3Ni_2O_7$. Nat Commun 16, 6560 (2025). C. Lu et al., Nat. Rev. Phys. **7**, 86 (2025).

22. K. J Choi, M. Biegalski, Y. L. Li, A. Sharan, J. Schubert, R. Uecker, P. Reiche, Y. B. Chen, X. Q. Pan, V. Gopalan, L. Q. Chen, D. G. Schlom, and C. B. Eom. Enhancement of Ferroelectricity in Strained $BaTiO_3$ Thin Films. Science 306 (5698) (2004).

23. M. Sutton, S. Mochrie, T. Greytak, S. E. Nagler, L. E. Berman, G. A. Held and G. B. Stephenson. Observation of speckle by diffraction with coherent X-rays. Nature 352, 608–610 (1991).

24. X. Yu, L. Wu, Y. Lin, J. Diao, J. Liu, J. Hallmann, U. Boesenberg, W. Lu, J. Möller, M. Scholz, A. Zozulya, A. Madsen, T. Assefa, E. S. Bozin, Y. Cao, H. You, D. Sheyfer, S. Rosenkranz, S. D. Marks, P. G. Evans, D. A. Keen, X. He, I. Božović, M. P. M. Dean, S. Yoo, and I. K. Robinson. Ultrafast Bragg coherent diffraction imaging of epitaxial thin films using deep complex-valued neural networks. npj Comput Mater 10, 24 (2024).

25. L. Wu, Y. Shen, A. M. Barbour, W. Wang, D. Prabhakaran, A. T. Boothroyd, C. Mazzoli, J. M. Tranquada, M. P. M. Dean, and I. K. Robinson. Real Space Imaging of Spin Stripe Domain Fluctuations in a Complex Oxide. Phys. Rev. Lett. 127, 275301(2021).

26. I. K. Robinson, and R. Harder. Coherent X-ray diffraction imaging of strain at the nanoscale. Nat Mater. 8 291-8 (2009)

27. H. M. Quiney. Coherent diffractive imaging using short wavelength light sources. Journal of Modern Optics, 57 1109–1149 (2010).

28. Z. Li, W. Guo, T. T. Zhang, J. H. Song, T. Y. Gao, Z. B. Gu, and Y. F. Nie. Epitaxial growth and electronic structure of Ruddlesden–Popper nickelates ($La_{n+1}Ni_nO_{3n+1}$, $n = 1–5$). APL Mater. 8 091112 (2020).

29. T. Cui, S. Choi, T. Lin, C. Liu, G. Wang, N. Wang, S. Chen, H. Hong, D. Rong, Q. Wang, Q. Jin, J. -O. Wang, L. Gu, C. Ge, C. Wang, J.-G. Cheng, Q. Zhang, L. Si, K.-J. Jin, and E.-J. Guo. Strain-mediated phase crossover in Ruddlesden–Popper nickelates. *Commun Mater* 5, 32 (2024).

30. G. A. Pan, Q. Song, D. F. Segedin, M.-C. Jung, H. El-Sherif, E. E. Fleck, B. H. Goodge, S. Doyle, D. C. Carrizales, A.T. N'Diaye, P. Shafer, H. Paik, L. F. Kourkoutis, I. El Baggari, A. S. Botana, C. M. Brooks, and J. A. Mundy. Synthesis and electronic properties of $Nd_{n+1}Ni_nO_{3n+1}$ Ruddlesden-Popper nickelate thin films. Phys. Rev. Materials 6, 055003 (2022).

31. D. Ferenc Segedin, B. H. Goodge, G. A. Pan, Q. Song, H. LaBollita, M.-C. Jung, H. El-Sherif, S. Doyle, A. Turkiewicz, N. K.Taylor, J. A. Mason, A.T.N'Diaye, H. Paik, I. El Baggari, A. S. Botana, L. F. Kourkoutis, C. M. Brooks, and J. A. Mundy, Limits to the strain engineering of layered square-planar nickelate thin films. Nat Commun 14, 1468 (2023).

32. M. Osada, C. Terakura, A. Kikkawa, M. Nakajima, H. -Y. Chen, Y. Nomura, Y. Tokura, and A. Tsukazaki. Strain-tuning for superconductivity in $La_3Ni_2O_7$ thin films. Commun Phys 8, 251 (2025).

33. U. Pietsch, V. Holý, and T. Baumbach. High-Resolution X-Ray Scattering: From Thin Films to Lateral Nanostructures. 2nd ed., Springer, (2004). DOI:10.1007/978-1-4757-4050-9.

34. A. Zabilska, A. H. Clark, D. Ferri, M. Nachtegaal, O. Kröcher, and O. V. Safonova. Beware of beam damage under reaction conditions: X-ray induced photochemical reduction of supported $VO_x$ catalysts during in situ XAS experiments. Phys. Chem. Chem. Phys. 24 21916-21926 (2022).

35. A. M. Maiden and J. M. Rodenburg. An improved ptychographical phase retrieval algorithm for diffractive imaging. Ultramicroscopy 109, 1256 (2009).

36. S. Takazawa, J. Kang, M. Abe, H. Uematsu, N. Ishiguro, and Y. Takahashi. Demonstration of single-frame coherent X- ray diffraction imaging using triangular aperture: Towards dynamic nanoimaging of extended objects. Optics Express 29 14394 (2021).